PHOTONICS Research

Two-dimensional tin diselenide nanosheets pretreated with an alkaloid for near- and mid-infrared ultrafast photonics

Zhenhong Wang,[1,†] Bin Zhang,[1,†] Bing Hu,[1] Zhongjun Li,[1] Chunyang Ma,[1] Yu Chen,[1] Yufeng Song,[1] Han Zhang,[1] Jun Liu,[1,*] and Guohui Nie[1,2]

[1]Shenzhen Engineering Laboratory of Phosphorene and Optoelectronics; Institute of Translational Medicine, Department of Otolaryngology, Shenzhen Second People's Hospital, The First Affiliated Hospital of Shenzhen University, Health Science Center; International Collaborative Laboratory of 2D Materials for Optoelectronics Science and Technology of Ministry of Education, College of Physics and Optoelectronic Engineering, Shenzhen University, Shenzhen 518060, China
[2]e-mail: nghui@21cn.com
*Corresponding author: liu-jun-1987@live.cn

Received 21 May 2020; revised 12 August 2020; accepted 9 September 2020; posted 11 September 2020 (Doc. ID 398203); published 12 October 2020

Two-dimensional (2D) tin diselenide ($SnSe_2$), a novel layered material with excellent optical and electronic properties, has been extensively investigated in various promising applications, including photodetectors, optical switching, and ultrafast photonics. In this work, $SnSe_2$ nanosheets have been obtained after pretreatment in an alkaloid, exhibiting high optical absorption and electron-enriched properties. Besides, the performances of the prepared $SnSe_2$ in near-infrared (NIR) and mid-infrared (MIR) ultrafast photonics are presented. Notably, by employing the $SnSe_2$-deposited microfiber device as a saturable absorber (SA) exhibiting typical nonlinear optical absorption properties, stable ultrashort pulses and rogue waves are realized in an erbium-doped fiber laser. Furthermore, the $SnSe_2$-deposited SA device is also applied to a thulium-doped fiber laser to achieve stable ultrashort pulses. This study indicates that $SnSe_2$ is expected to be a suitable candidate for ultrafast fiber lasers in the NIR and MIR regions.

https://doi.org/10.1364/PRJ.398203

1. INTRODUCTION

2D materials have extensively served as promising materials for optoelectronic fields such as photodetectors [1], optical switches [2], optical modulators [3,4], and saturable absorbers (SAs) [5–7]. The family of 2D materials that have been widely demonstrated recently due to their promising potential in ultrafast photonics, include graphene, graphdiyne, black phosphorus (BP), MXene, topological insulators (TIs), and transition metal dichalcogenides (TMDs). Recently, as a kind of typical TMD, $SnSe_2$ has attracted considerable research interest because of its excellent electrical and optical properties. Besides, $SnSe_2$ possesses a direct band gap from 1.84 to 2.04 eV and an indirect band gap from 1.07 to 1.69 eV based on its layered-sensitive features [8]. In addition, $SnSe_2$ exhibits excellent nonlinear optical properties (NOPs), which can be used as promising SAs in the broadband regions [9–14]. However, only *Q*-switched operation has been successfully demonstrated using the $SnSe_2$ SA in the 2 μm mid-infrared (MIR) region. Therefore, it is imperative and significant to further investigate the nonlinear optical properties of the new 2D material $SnSe_2$ and its application in ultrafast photonics in the near-infrared (NIR) and MIR wavelength regions.

Ultrafast fiber lasers have been widely used in industries and scientific research fields [15,16] and have generated enormous economic and social benefits. The passive mode-locking technique using 2D materials as SAs is generally considered one of the most efficient approaches to obtain ultrashort pulses in ultrafast fiber lasers. At present, the majority of mode-locked fiber lasers based on 2D material SAs are concentrated on ultrashort pulse generation in the NIR range (1–1.5 μm). It is interesting to note that the ultrafast pulse fiber lasers operating in the MIR region (2–3.5 μm) have exhibited potential applications such as optical communication [17], supercontinuum generation [18], and laser radar [19]. Therefore, it is essential to explore and investigate the available 2D materials with unique nonlinear absorption features in the MIR region. In addition, ultrafast fiber lasers are the ideal platform for studying soliton dynamics [20–22]. At present, there are multiple types of soliton phenomena reported in ultrafast fiber lasers, including soliton explosion [23], soliton pulsation [24], soliton molecules [25], and

rogue waves (RWs) [26]. RWs are unpredicted rare wave packets with extreme amplitudes, which have gained substantial interest in many fields of science [26] like oceanography, optics, and economics. Furthermore, the exploration of RWs is favorable to the achievement of high-energy pulses [27]. Now, optical RWs have been demonstrated in various nonlinear optical systems, such as optical fibers [28], Raman amplifiers [29], solid-state lasers [30], and ultrafast fiber lasers [31]. Generally, the collisions and interactions of multiple solitons play a major role in generating optical RWs [32,33]. Moreover, the combined effects of multiple pulses and strong nonlinear interactions are an effective impetus in optical RW formation [34,35]. Recently, it has been found that these 2D materials possess high NOPs, exhibiting enormous potential in optical RWs. Besides, the 2D material SA device on microfiber shows a unique structure, greatly enhancing the highly nonlinear effects for the fiber laser by the effective interaction length between the propagating light and 2D materials [36]. Thus, ultrafast fiber lasers with 2D material SA microfiber devices can provide an excellent playground for studying optical RWs. However, to our knowledge, there have been rare reports on RWs based on 2D material SAs.

In this study, $SnSe_2$ nanosheets pretreated with urea (economic, environmentally friendly, mild alkalinity and reducing ability) were fabricated, the corresponding $SnSe_2$-deposited microfiber devices were made, and their nonlinear optical absorption characteristics in the broadband region were investigated. Furthermore, based on the $SnSe_2$-deposited microfiber SA device, the passive mode-locking operation is realized for the 1.55 and 2 μm fiber lasers. More importantly, RW generation is observed in the 1.55 μm fiber laser. To our knowledge, this is the first report of RWs in 1.55 μm fiber lasers with a $SnSe_2$-based SA. These experimental results show that $SnSe_2$ can be utilized as potential SAs in NIR and MIR ultrafast photonics, opening a promising way for nonlinear photonic devices with $SnSe_2$.

2. PREPARATION, CHARACTERIZATION, AND NONLINEAR OPTICAL PROPERTIES OF $SnSe_2$ NANOSHEETS

Few-layered $SnSe_2$ materials were obtained via the liquid exfoliation method after pretreatment in different aqueous media to obtain nanosheets with good stability and narrow size distribution. The ultrathin $SnSe_2$ nanosheets were prepared by the liquid exfoliation of bulk $SnSe_2$ crystal. Briefly, 50 mg of bulk $SnSe_2$ was first ground by hand and then dispersed in deionized water with different additives (blank, 1 mg $AgNO_3$, 2 mg urea, and 2 mg NaOH). Sonication was then performed for 20 min with an ice/water bath. After that, the brown suspension was kept under 3000 r/min centrifugation for 5 min to remove the unexfoliated $SnSe_2$. The suspension was further centrifuged with deionized water for 5 min at 12,000 r/min, and the precipitate was redispersed in desired solvent prior to use. It has been reported that alkali and metal cations would enhance the resistance against water and oxygen [37,38], and thus water, an aqueous solution of sodium hydroxide (NaOH), urea, and silver nitrate ($AgNO_3$) were used for screening a most promising solvent. Urea was selected because of its controllable hydrolysis process to smartly produce OH^- and its mild reducing ability, which might strengthen the resistance against oxygen [39,40]. As depicted in Fig. 1(a), all the $SnSe_2$ products exhibited broad absorption behavior, covering the NIR and MIR regions. It is noteworthy that at the same concentration, $SnSe_2$ pretreated with urea, demonstrated much higher absorption, indicating higher stability against water and O_2 under the sonication process, which is more promising for optical applications. Furthermore, the dynamic light scattering result [Fig. 1(b)] suggests that the $SnSe_2$ nanosheets have the narrowest size distribution and highest intensity, confirming that the urea treatment facilitates the formation of uniformly structured $SnSe_2$ nanosheets. It is proposed that the reducibility of urea might inhibit the oxidative decomposition of $SnSe_2$ and promotes the charge transfer between urea and $SnSe_2$, the results of which enhance the stability dramatically.

Then the geometric and electronic structures of the nanosheets treated with urea were carefully characterized with transmission electron microscope (TEM), energy-dispersive X-ray spectroscopy (EDXS), Raman and X-ray photoelectron spectroscopy (XPS), and the results are shown in Figs. 2 and 3, respectively. As shown in Fig. 2(a), the distances between neighboring atoms are 0.270 nm and 0.382 nm, which matched well with the crystal files in Fig. 2(c). In addition, the fast Fourier transform (FFT) pattern in Fig. 2(b) exhibits six-fold-symmetric spots, confirming that the obtained $SnSe_2$ has

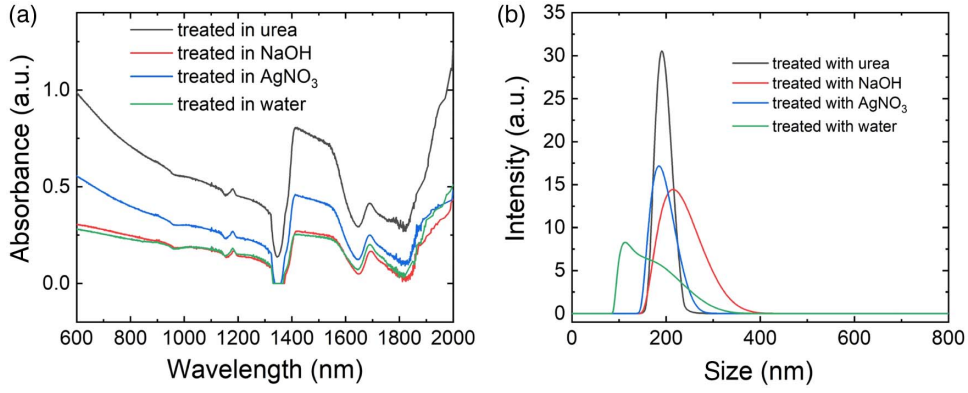

Fig. 1. Screening of pretreatment procedures. (a) Absorption spectra and (b) dynamic light scattering (DLS) spectra of a 0.01 mg/mL $SnSe_2$ aqueous solution with different pretreatments.

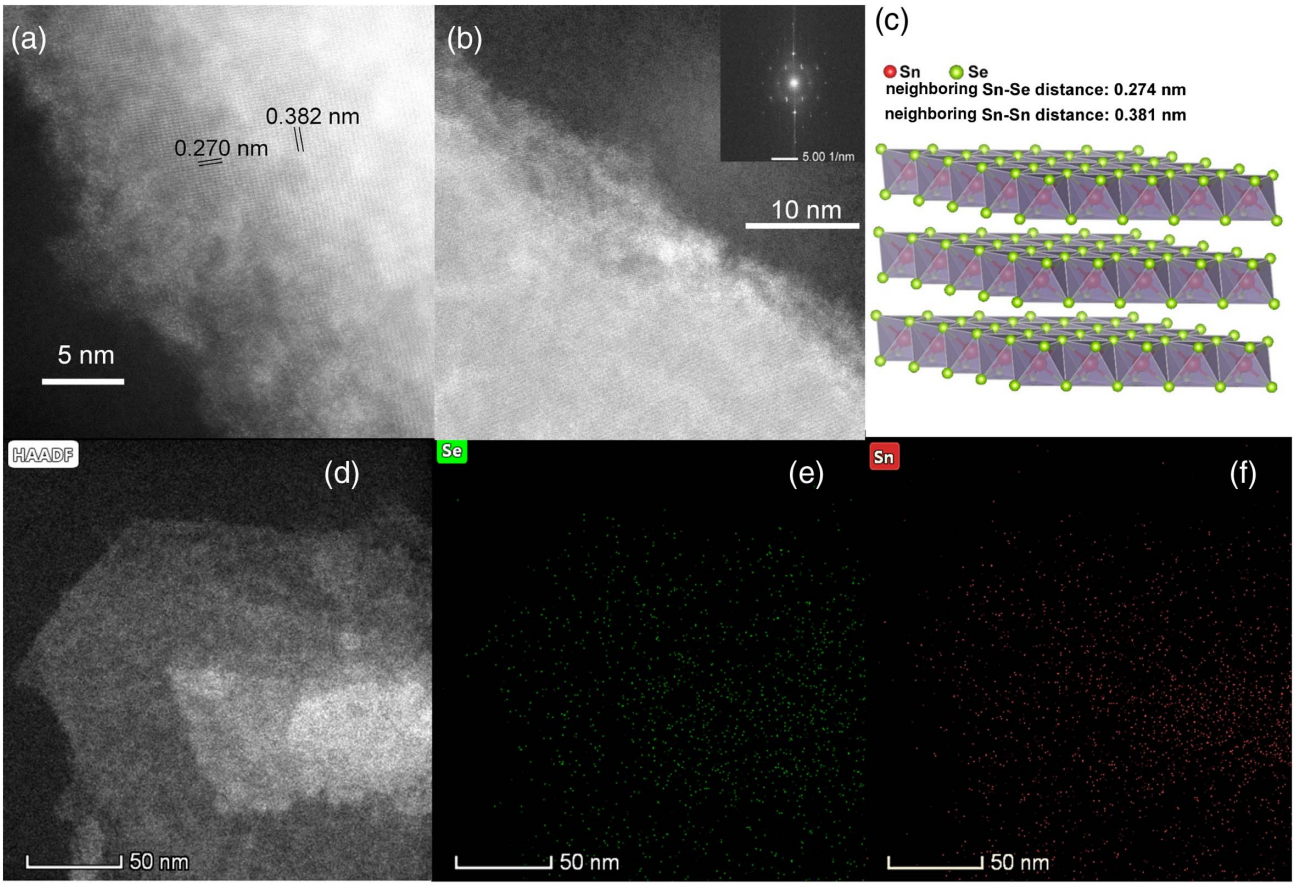

Fig. 2. (a), (b) HAADF-STEM images, (c) crystal model, (d)–(f) EDXS results of $SnSe_2$ nanosheets pretreated with urea.

a hexagonal structure. Figures 2(d)–2(f) suggest that Sn and Se elements were well distributed across the whole structure, and the quantitative analysis indicates that the atomic ratio of Se to Sn is 1.97, which is quite close to the exact value of 2. The intact structure of $SnSe_2$ and the crystalline configuration were maintained, with each Sn atom coordinated with six Se atoms, despite the urea treatment.

Figures 3(a)–3(c) depict the XPS result of the obtained $SnSe_2$ nanosheets. It is noteworthy that for Se 3d electrons, there are two sets of binding energy values, 53.6 eV and 51.8 eV, respectively. It has been reported that 53.6 eV is usually observed for $SnSe_2$, so the unexceptionally low binding energy of 51.8 eV should be ascribed to the electron donation from urea, making the nanosheets electron enriched, which lays a good foundation for the electron–photon interactions. The Raman spectrum [Fig. 3(d)] further illustrates the vibration configurations, clearly suggesting that the E_g and A_{1g} vibration modes were kept regardless of the thickness. The redshift of the E_g mode was attributed to the decrease of layer numbers, and the position of the A_{1g} vibration did not change obviously, which is consistent with the previously reported results and confirmed that the treatment of urea did not damage the integrity of the structure [41,42]. With intact geometric structure and admirable electron properties, the $SnSe_2$ nanosheets are promising for various electronic and photonic applications.

The prepared $SnSe_2$ nanosheets were dissolved into the ethanol solution with a concentration of 0.1 mg/mL. The microfiber was drawn by using the flame brushing technique, and its diameter was ~12 μm. Then the $SnSe_2$ solution was dripped onto the microfiber and the light was injected into the microfiber to deposit the $SnSe_2$ samples onto the microfiber. By using this method, the $SnSe_2$-deposited microfiber device was fabricated. The corresponding nonlinear optical absorption property was studied by utilizing the two-detector equipment. The pulse fiber lasers (1557 nm, 500 fs, 98 MHz; 1890 nm, 1 ps, 5.9 MHz) were used as optical sources. The measured results are illustrated in Fig. 4. As can be seen from the figure, the $SnSe_2$ SA devices exhibit typical saturable absorption characteristics. The modulation depth (ΔT) and nonsaturable loss (α_{ns}) of the $SnSe_2$ SA device at 1.55 μm are 14.5% and 82.5%, respectively. The corresponding ΔT and α_{ns} at 2 μm are 17.9% and 78.8%, respectively. These results indicate that the fabricated $SnSe_2$-deposited SA devices can be applied to mode locking in the 1.55 μm and 2 μm regions.

3. EXPERIMENTAL SETUP

The fiber lasers [erbium-doped fiber laser (EDFL) and thulium-doped fiber laser (TDFL)] built in this experiment have similar cavity diagrams as shown in Fig. 5. The typical fiber laser consists of a pump laser, a wavelength-division multiplexer (WDM), gain fibers (3 m EDF or 2.7 m TDF), an optical coupler (OC), a $SnSe_2$-based SA, a polarization controller (PC), and a polarization-independent isolator (PI-ISO).

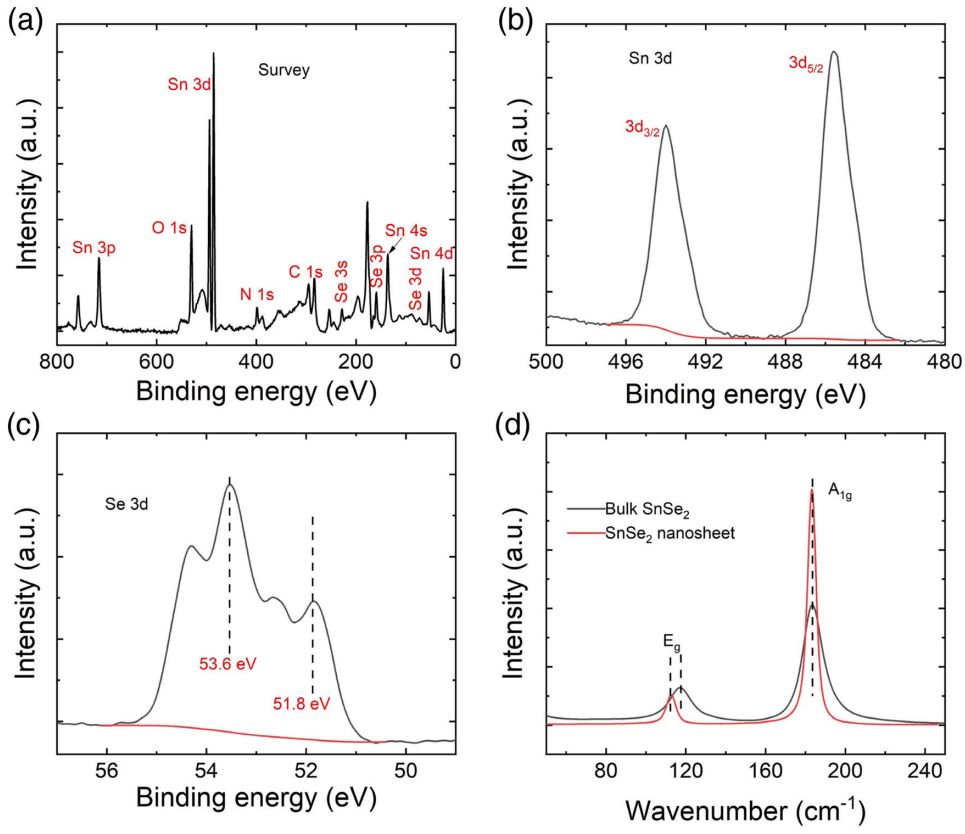

Fig. 3. (a)–(c) XPS profiles and (d) Raman spectrum of $SnSe_2$ nanosheets.

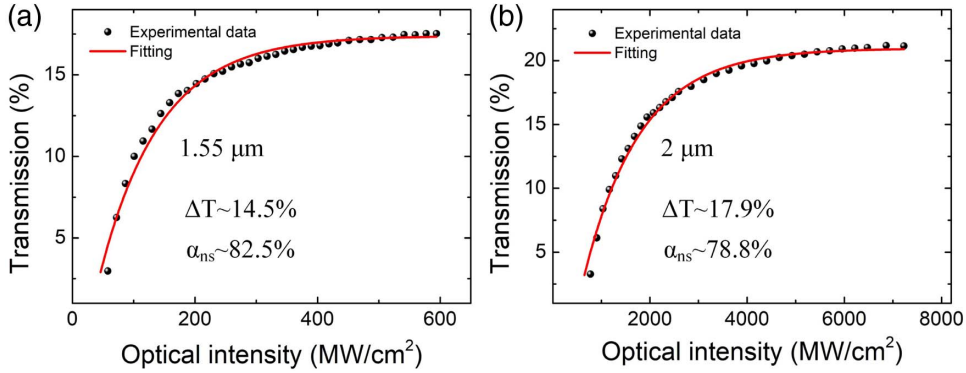

Fig. 4. NOPs of $SnSe_2$ SA devices at (a) 1.55 μm and (b) 2 μm.

For EDFL and TDFL, the pump lasers operate at 980 nm and 1570 nm, respectively. In the EDFL, the 30% port of the 30/70 OC is used for output detection. In the TDFL, the 20% port of the 20/80 OC is used for output detection. The cavity lengths of the EDFL and TDFL are 18.5 m and 33.4 m, respectively. For the EDFL and TDFL, the total net cavity dispersions are ~ -0.173 ps^2 at 1.55 μm and ~ -2.31 ps^2 at 1.9 μm, respectively. The optical spectrum analyzers (Yokogawa AQ6370D for the EDFL and Yokogawa AQ6375B for the TDFL) are used to observe the optical spectrum of the output pulses. The pulse characteristics are measured by using an oscilloscope with a 1 GHz bandwidth and a photodetector. Furthermore, the temporal trains of the chaotic pulses at 1.55 μm are evaluated by use of an 18.5 ps photodetector and a real-time oscilloscope with a 20 GHz bandwidth. The radio-frequency (RF) spectrum analyzer is used for recording the RF spectrum of the output pulses. The corresponding pulse duration is measured by using a commercial autocorrelator (APE PulseCheck).

4. ULTRAFAST PHOTONICS APPLICATIONS

A. Stable Ultrashort Pulses in the EDFL

The fabricated $SnSe_2$-deposited SA is added into the EDFL cavity. By gradually increasing the pump power and properly changing the cavity polarization state, the stable ultrashort

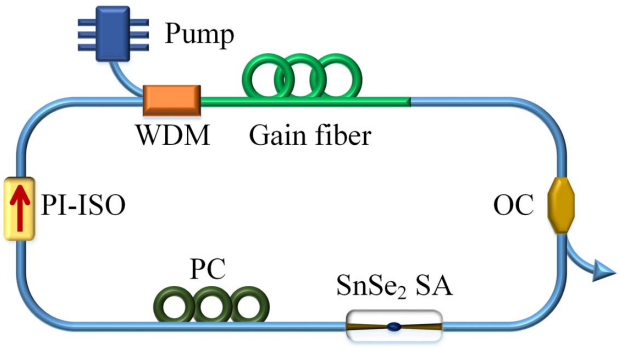

Fig. 5. Schematic diagram of the typical mode-locked fiber laser (for EDFL or TDFL).

pulses in the fundamental repetition rate (RPR) state can be obtained as illustrated in Fig. 6. The output spectrum is displayed in Fig. 6(a). The central wavelength and full width at half-maximum (FWHM) are 1560.14 nm and 5.03 nm, respectively. In addition, some Kelly sidebands are clearly observed, suggesting that the EDFL operates in the soliton mode-locking state. Figure 6(b) displays the recorded pulse trains, and the pulse-to-pulse separation is about 92.3 ns, which corresponds to an RPR of 10.83 MHz. The pulse width measured by using autocorrelation equipment is presented in Fig. 6(c). The FWHM of the output pulses is approximately 922.7 fs, corresponding to a pulse duration of ~598 fs if sech^2 fitting is assumed. Therefore, the estimated time bandwidth product (TBP) is ~0.371, suggesting that the ultrashort pulse is near transform limited. Figure 6(d) illustrates the measured RF spectrum. Obviously, there is a peak located at 10.83 MHz with the signal-noise-ratio (SNR) of ~73.3 dB, suggesting that the mode-locking operation is under a relatively high stability.

B. Chaotic Multiple Pulses in the EDFL

After achievement of stable ultrashort pulses, the pump power is further increased. The chaotic multiple-pulse state starts to appear at the pump power of 320 mW by slightly changing the PC. Figure 7 displays the output characteristics of chaotic pulses at the pump power of 400 mW. Obviously, there are some Kelly sidebands distributed on both sides of the spectrum as illustrated in Fig. 7(a). A high-speed oscilloscope (20 GHz) is used to measure the pulse trains of these chaotic pulses as depicted in Fig. 7(b). Close-ups of the single pulse packet are illustrated in Fig. 7(c). There are many small pulses with chaotic and random intensities observed in this packet. The pulse interval is ~92.3 ns, corresponding to the round-trip time determined by the cavity length. Besides, a relatively low-speed oscilloscope (1 GHz) is used to measure the temporal trains as presented in the inset of Fig. 7(b). These pulse trains can only reflect the total intensity of chaotic pulses, and the corresponding fine structure cannot be resolved. In addition, their intensity amplitudes are evaluated by utilizing a high-speed oscilloscope (20 GHz). Figure 7(d) depicts the measured intensity histogram, showing a non-Gaussian statistical distribution. Then we also calculated the significant wave height (SWH), which is defined as the mean amplitude of the highest third of the packets. Generally, the criteria for RW generation in the laser systems are based on the fact that its amplitude is more than twice the SWH [26,31]. The calculated SWH is about 44.1 mV as illustrated in Fig. 7(d). The measured highest amplitude (MHA) is ~160 mV, which is ~3.6 times the SWH, indicating that the RWs can be generated from the chaotic

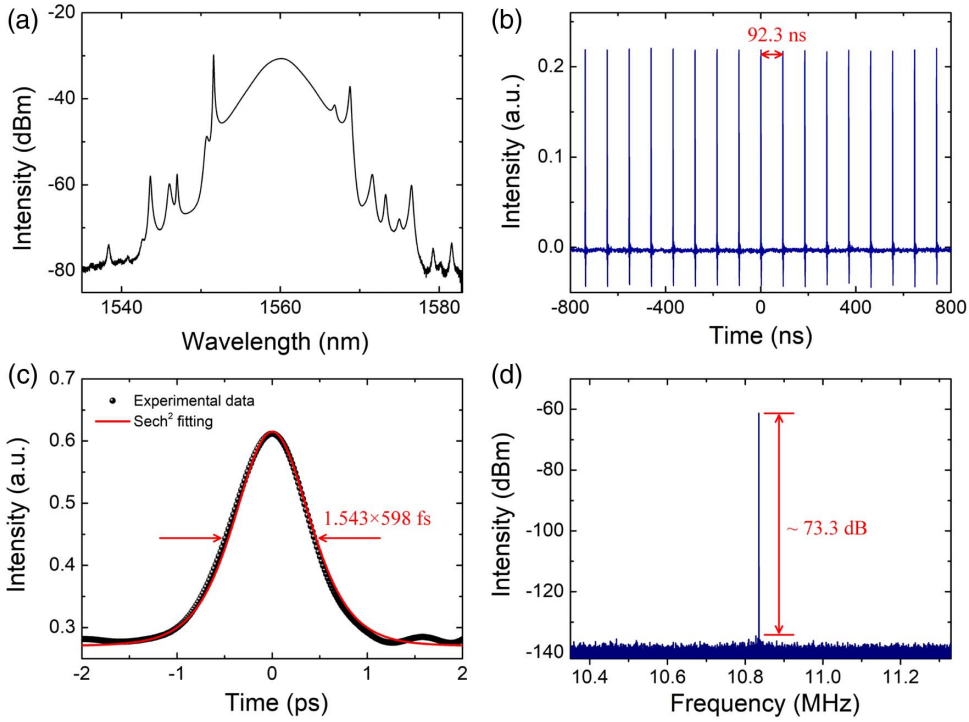

Fig. 6. Stable ultrashort pulse operation: (a) optical spectrum, (b) oscilloscope trace, (c) autocorrelation trace, and (d) frequency spectrum.

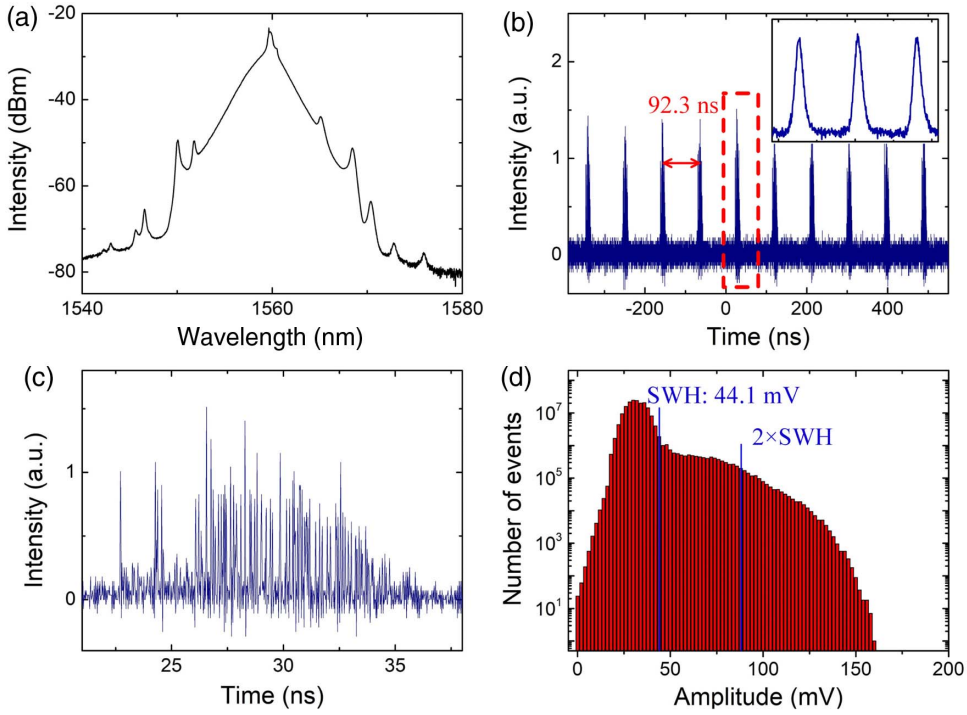

Fig. 7. Chaotic multiple pulse operation: (a) optical spectrum, (b) high-speed oscilloscope trace (inset: low-speed oscilloscope trace), (c) enlarged view of the selected dashed part in (b), and (d) statistical histogram.

pulses. In order to show the evolution of RW generation, the evolution process of chaotic pulses at successive cavity round-trips is displayed in Fig. 8. As can be seen from this figure, the chaotic pulse packets have different amplitudes, which can fluctuate randomly from time to time. For example, the situations of these peaks (Peak 1, Peak 2, Peak 3, Peak 4, Peak 5, and Peak 6) are obviously different. In addition, the corresponding intensities are also different. Actually, these situations and intensities vary at random.

Furthermore, the intensity histograms of chaotic pulses at the pump powers of 500 mW and 600 mW are studied as shown in Fig. 9. As can be seen from these intensity histograms, the statistical distributions are non-Gaussian. Besides, the calculated SWH at 500 mW is about 61.5 mV. The corresponding MHA is ~198 mV, which is more than twice the SWH. The MHA at the pump power of 600 mW is ~273 mV, which is also more than twice the SWH (76.6 mV). Moreover, in order to confirm the role of the $SnSe_2$ material, the $SnSe_2$-based microfiber photonic device is replaced by microfiber without deposition. However, no matter how the pump power and PC are adjusted in the fiber laser, neither the stable ultrashort pulses nor the chaotic pulses are obtained. Therefore, it can be concluded that the $SnSe_2$ material can play a key role in the generation of ultrashort pulses and chaotic pulses. Moreover, the $SnSe_2$-based microfiber photonic device is replaced by the $SnSe_2$ SA with a sandwiched structure on the fiber connector. But, no matter how the PC and pump power are changed in the fiber laser, the chaotic pulses cannot be obtained. Actually, in addition to presenting the excellent saturable absorption, the $SnSe_2$-based microfiber photonic device also brings a highly nonlinear effect for the EDFL cavity with the evanescent field interaction between the propagation light and the $SnSe_2$ material [34–36], greatly facilitating the generation of chaotic multiple pulses.

Besides, in order to investigate the effect of the polarization directions on chaotic pulses under low pump power, the pump power is set to 200 mW. By continuously adjusting the polarization directions, the chaotic pulses can also be obtained as illustrated in Fig. 10. However, the optical spectrum in Fig. 10(a) is different from the one in Fig. 7(a). Obviously, the situation of the central peaks is different. The temporal trains based on the high-speed oscilloscope are illustrated in Fig. 10(b). The pulse spacing between adjacent pulses is ~92.3 ns, and the intensity in single chaotic pulse packet varies randomly. In addition, compared with the chaotic pulses in Fig. 7(c), there are fewer pulses in the chaotic pulse packet in Fig. 10(c). Furthermore, the temporal separation among these adjacent pulses is relatively larger. As illustrated in Fig. 10(d), the calculated SWH is about 63 mV. The measured highest amplitude is ~221 mV, which is ~3.5 times the SWH, indicating that the RWs can be generated. These experiment results indicate that the RWs can be generated under low pump power and different polarization directions, which is consistent with the previous observation in the report [31].

C. Stable Ultrashort Pulses in the TDFL

In the TDFL, we can also achieve stable mode-locked pulses at 2 μm by using the $SnSe_2$-based SA device. At a pump power of 300 mW, continuous-wave (CW) emission begins to appear. By further increasing the pump power and properly setting the PC, stable mode locking can be observed as presented in Fig. 11. The optical spectrum of the output pulses is

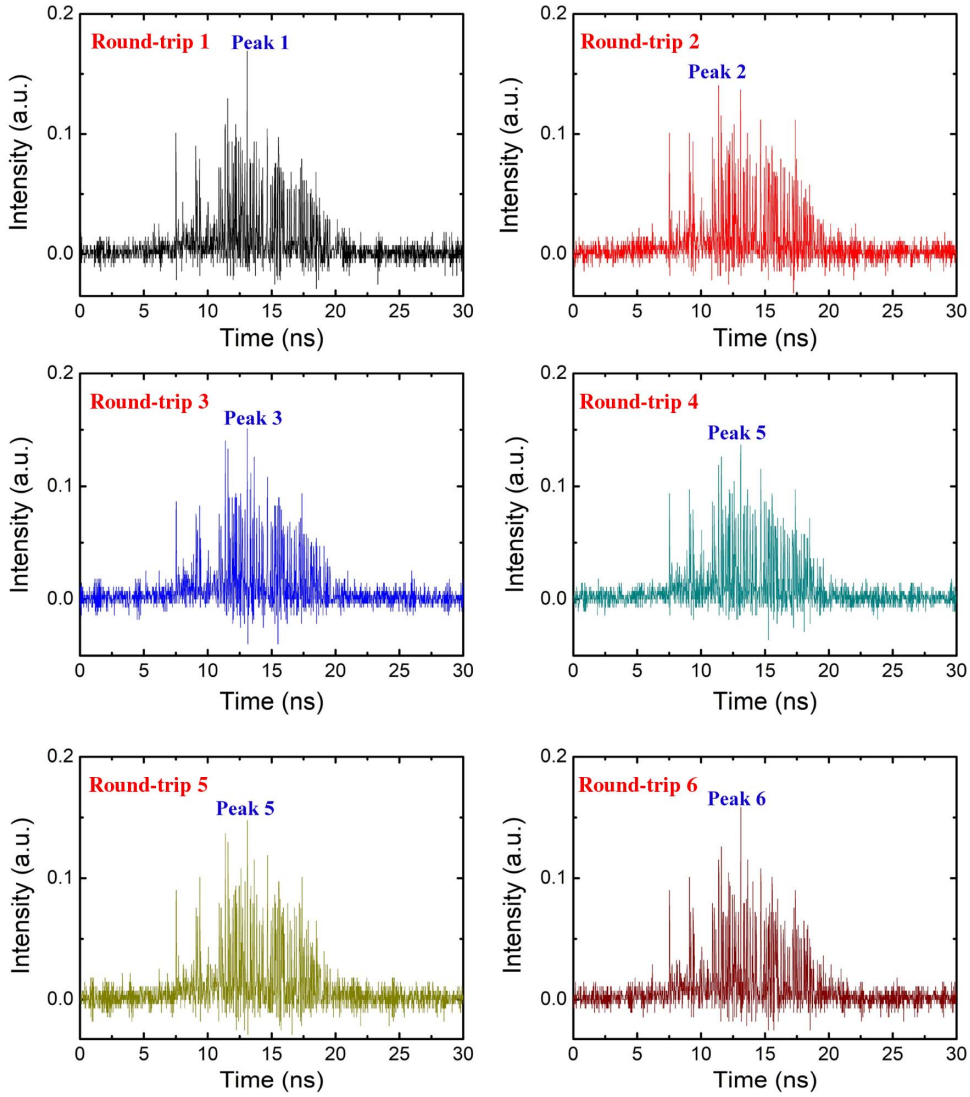

Fig. 8. Evolution of chaotic multiple pulses.

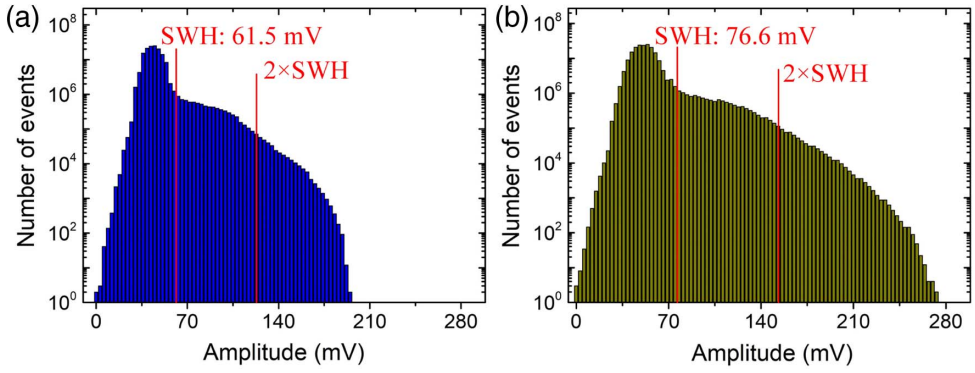

Fig. 9. Intensity histograms of chaotic pulses at (a) 500 mW and (b) 600 mW.

presented in Fig. 11(a). The corresponding central wavelength and FWHM are 1881.27 nm and 2.09 nm, respectively. Besides, typical Kelly sidebands, characteristic dips, and sub-sidebands are observed on the spectrum. These dips come from the water absorption line in air at 2 μm. The sub-sidebands are associated with the sidebands of the vector solitons [43,44], and similar observations are also demonstrated in previous reports [45–47]. Figure 11(b) displays the pulse trains with a pulse

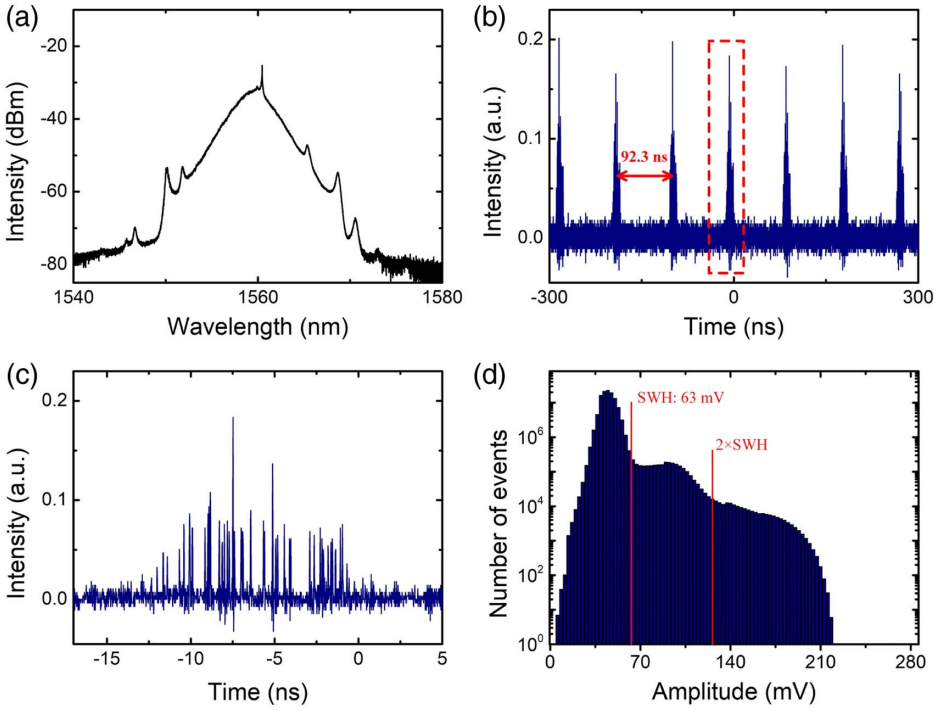

Fig. 10. Chaotic multiple pulse operation at 200 mW: (a) optical spectrum, (b) high-speed oscilloscope trace, (c) enlarged view of the selected dashed part in (b), and (d) statistical histogram.

interval of 166.7 ns. The recorded autocorrelation curve is shown in Fig. 11(c). The pulse duration is about 2.06 ps after a sech^2 fitting. The corresponding TBP of the output pulses is estimated to be ~0.364, indicating that they are chirped pulses. Figure 11(d) depicts the measured RF spectrum. The high peak is located at 6 MHz and the SNR is more than 68 dB, indicating that the laser operation is relatively stable. In addition, the output power of the output pulses exhibits a linear increment with the increase of pump power as displayed in Fig. 11(e). The corresponding maximum power is approximately 42.75 mW. Besides, the optical spectra of output pulses at different hours are also recorded as illustrated in Fig. 11(f). It is obvious that the overall wavelength shape and spectral intensity remain relatively stable at several hours, which indicates that the mode locking based on the $SnSe_2$-deposited SA has a relatively good stability. Finally, the output performances of the TDFLs based

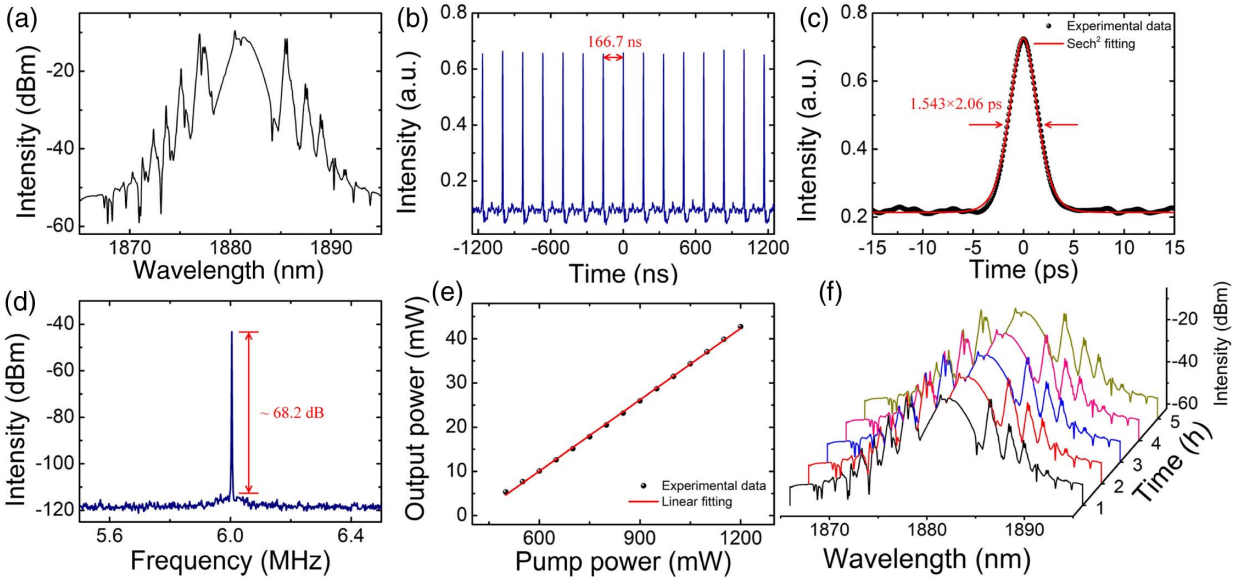

Fig. 11. Output performance of the TDFL with a $SnSe_2$-deposited SA: (a) optical spectrum, (b) oscilloscope trace, (c) autocorrelation trace, (d) frequency spectrum, (e) relationship between pump power and output power, and (f) optical spectra with different hours.

Table 1. Output Results of the 2 μm Fiber Lasers Based on Different 2D Material SAs

Material	Wavelength [nm]	ΔT [%]	Width [ps]	SNR [dB]	Output [mW]	Refs.
Graphene	1953.3	4	2.1	50	1.41	[48]
BP	1910	4.1	0.739	>70	1.5	[49]
Bi_2Te_3	1909.5	9.8	1.26	52	<3	[50]
WSe_2	1863.96	1.83	1.16	53	32.5	[51]
GeTe	1931.15	8.3	0.983	87.6	35	[52]
Graphdiyne	1880.3	27.1	2.52	63.3	36.4	[53]
$SnSe_2$	1881.27	17.9	2.06	68.2	42.75	This work

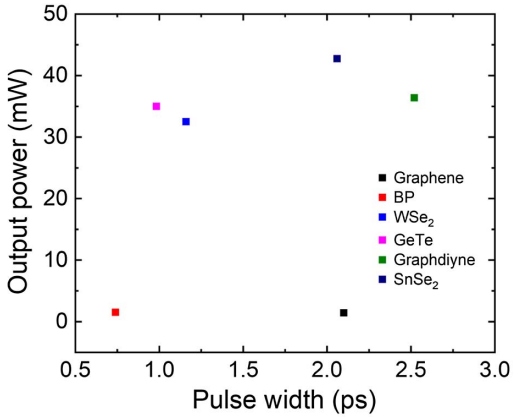

Fig. 12. Graphical comparison of TDFL with different 2D materials.

on different 2D material SAs are summarized in Table 1 and Fig. 12. It can be seen that the TDFL with $SnSe_2$-deposited SA exhibits similar output pulse characteristics, indicating that $SnSe_2$ exhibits promising potential in ultrafast photonics at 2.0 μm.

5. CONCLUSION

In summary, the ultrafast laser applications of $SnSe_2$ pretreated with urea as an SA in the NIR and MIR regions have been demonstrated. Owing to its excellent saturable absorption properties, $SnSe_2$ is deposited on a microfiber to fabricate the SA. By incorporating the $SnSe_2$-based SA into the EDFL cavity, RWs are obtained. Furthermore, a mode-locked TDFL with the $SnSe_2$-based SA is also reported for the first time. The stable ultrashort pulses are obtained with a central wavelength of 1881.27 nm and a pulse width of 2.06 ps. The maximum average output power is 42.75 mW. These experimental results reveal that $SnSe_2$ has promising potential in applications of ultrafast photonics in the NIR and MIR wavelength regions, greatly promoting further investigation for new 2D materials in ultrafast optics fields.

Funding. Science, Technology and Innovation Commission of Shenzhen Municipality (JCYJ20190806163805286, JCYJ20190808143813399); Taipei University of Technology–Shenzhen University Joint Research Program (2020007); Natural Science Foundation of Guangdong Province (2019A1515111060, 2020A151501787); China Postdoctoral Science Foundation (2019M660212); National Natural Science Foundation of China (61705140, 61805115, 61875132, 61875138).

Disclosures. The authors declare no conflicts of interest.

†These authors contributed equally to this work.

REFERENCES

1. F. H. L. Koppens, T. Mueller, P. Avouris, A. C. Ferrari, M. S. Vitiello, and M. Polini, "Photodetectors based on graphene, other two-dimensional materials and hybrid systems," Nat. Nanotechnol. **9**, 780–793 (2014).
2. M. Ono, M. Hata, M. Tsunekawa, K. Nozaki, H. Sumikura, H. Chiba, and M. Notomi, "Ultrafast and energy-efficient all-optical switching with graphene-loaded deep-subwavelength plasmonic waveguides," Nat. Photonics **14**, 37–43 (2020).
3. Z. Sun, A. Martinez, and F. Wang, "Optical modulators with 2D layered materials," Nat. Photonics **10**, 227–238 (2016).
4. Z. Xie, F. Zhang, Z. Liang, T. Fan, Z. Li, X. Jiang, H. Chen, J. Li, and H. Zhang, "Revealing of the ultrafast third-order nonlinear optical response and enabled photonic application in two-dimensional tin sulfide," Photon. Res. **7**, 494–502 (2019).
5. T. Jiang, K. Yin, C. Wang, J. You, H. Ouyang, R. Miao, C. Zhang, K. Wei, H. Li, H. Chen, R. Zhang, X. Zheng, Z. Xu, X. Cheng, and H. Zhang, "Ultrafast fiber lasers mode-locked by two-dimensional materials: review and prospect," Photon. Res. **8**, 78–90 (2020).
6. J. Liu, Y. Chen, Y. Li, H. Zhang, S. Zheng, and S. Xu, "Switchable dual-wavelength *Q*-switched fiber laser using multilayer black phosphorus as a saturable absorber," Photon. Res. **6**, 198–203 (2018).
7. H. Luo, X. Tian, Y. Gao, R. Wei, J. Li, J. Qiu, and Y. Liu, "Antimonene: a long-term stable two-dimensional saturable absorption material under ambient conditions for the mid-infrared spectral region," Photon. Res. **6**, 900–907 (2018).
8. J. M. Gonzalez and I. I. Oleynik, "Layer-dependent properties of SnS_2 and $SnSe_2$ two-dimensional materials," Phys. Rev. B **94**, 125443 (2016).
9. C. Cheng, Z. Li, N. Dong, J. Wang, and F. Chen, "Tin diselenide as a new saturable absorber for generation of laser pulses at 1 μm," Opt. Express **25**, 6132–6140 (2017).
10. R. Sun, H. Zhang, and N. Xu, "High-power passively *Q*-switched Yb-doped fiber laser based on tin selenide as a saturable absorber," Laser Phys. **28**, 085105 (2018).
11. Q. Hu, X. Zhang, Z. Liu, P. Li, M. Li, Z. Cong, Z. Qin, and X. Chen, "High-order harmonic mode-locked Yb-doped fiber laser based on a $SnSe_2$ saturable absorber," Opt. Laser Technol. **119**, 105639 (2019).
12. J.-S. Liu, X.-H. Li, Y.-X. Guo, A. Qyyum, Z.-J. Shi, T.-C. Feng, Y. Zhang, C.-X. Jiang, and X.-F. Liu, "$SnSe_2$ nanosheets for subpicosecond harmonic mode-locked pulse generation," Small **15**, 1902811 (2019).
13. M. Wang, Z. Wang, X. Xu, S. Duan, and C. Du, "Tin diselenide-based saturable absorbers for eye-safe pulse lasers," Nanotechnology **30**, 265703 (2019).

14. B. Ran, H. Sun, and Y. Ma, "Two-dimensional tin diselenide passively Q-switched 2 μm Tm:YAP laser," Infrared Phys. Technol. **105**, 103227 (2020).
15. M. E. Fermann and I. Hartl, "Ultrafast fibre lasers," Nat. Photonics **7**, 868–874 (2013).
16. J. Ma, Z. Qin, G. Xie, L. Qian, and D. Tang, "Review of mid-infrared mode-locked laser sources in the 2.0 μm–3.5 μm spectral region," Appl. Phys. Rev. **6**, 021317 (2019).
17. K. Anbarasi, C. Hemanth, and R. G. Sangeetha, "A review on channel models in free space optical communication systems," Opt. Laser Technol. **97**, 161–171 (2017).
18. D. D. Hudson, S. Antipov, L. Li, I. Alamgir, T. Hu, M. E. Amraoui, Y. Messaddeq, M. Rochette, S. D. Jackson, and A. Fuerbach, "Toward all-fiber supercontinuum spanning the mid-infrared," Optica **4**, 1163–1166 (2017).
19. W. Ni-Meister, W. Yang, S. Lee, A. H. Strahler, and F. Zhao, "Validating modeled lidar waveforms in forest canopies with airborne laser scanning data," Remote Sens. Environ. **204**, 229–243 (2018).
20. P. Grelu and N. Akhmediev, "Dissipative solitons for mode-locked lasers," Nat. Photonics **6**, 84–92 (2012).
21. Y. Song, X. Shi, C. Wu, D. Tang, and H. Zhang, "Recent progress of study on optical solitons in fiber lasers," Appl. Phys. Rev. **6**, 021313 (2019).
22. J. Liu, J. Wu, H. Chen, Y. Chen, Z. Wang, C. Ma, and H. Zhang, "Short-pulsed Raman fiber laser and its dynamics," Sci. China Phys. Mech. Astron. **64**, 214201 (2021).
23. M. Liu, T.-J. Li, A.-P. Luo, W.-C. Xu, and Z.-C. Luo, "'Periodic' soliton explosions in a dual-wavelength mode-locked Yb-doped fiber laser," Photon. Res. **8**, 246–251 (2020).
24. M. Liu, Z.-W. Wei, H. Li, T.-J. Li, A.-P. Luo, W.-C. Xu, and Z.-C. Luo, "Visualizing the 'invisible' soliton pulsation in an ultrafast laser," Laser Photon. Rev. **14**, 1900317 (2020).
25. T. Feng, D. Zhang, X. Li, Q. Abdul, Z. Shi, J. Lu, P. Guo, Y. Zhang, J. Liu, and Q. J. Wang, "SnS_2 nanosheets for Er-doped fiber lasers," ACS Appl. Nano Mater. **3**, 674–681 (2020).
26. Y. Song, Z. Wang, C. Wang, K. Panajotov, and H. Zhang, "Recent progress on optical rogue waves in fiber lasers: status, challenges, and perspectives," Adv. Photon. **2**, 024001 (2020).
27. N. Akhmediev, J. M. Soto-Crespo, and A. Ankiewicz, "How to excite a rogue wave," Phys. Rev. A **80**, 043818 (2009).
28. D. R. Solli, C. Ropers, P. Koonath, and B. Jalali, "Optical rogue waves," Nature **450**, 1054–1057 (2007).
29. K. Hammani, C. Finot, J. M. Dudley, and G. Millot, "Optical rogue-wave-like extreme value fluctuations in fiber Raman amplifiers," Opt. Express **16**, 16467–16474 (2008).
30. M. G. Kovalsky, A. A. Hnilo, and J. R. Tredicce, "Extreme events in the Ti:sapphire laser," Opt. Lett. **36**, 4449–4451 (2011).
31. C. Lecaplain, P. Grelu, J. M. Soto-Crespo, and N. Akhmediev, "Dissipative rogue waves generated by chaotic pulse bunching in a mode-locked laser," Phys. Rev. Lett. **108**, 233901 (2012).
32. N. Akhmediev, J. M. Soto-Crespo, and A. Ankiewicz, "Could rogue waves be used as efficient weapons against enemy ships?" Eur. Phys. J. Spec. Top. **185**, 259–266 (2010).
33. A. Demircan, S. Amiranashvili, C. Brée, C. Mahnke, F. Mitschke, and G. Steinmeyer, "Rogue events in the group velocity horizon," Sci. Rep. **2**, 850 (2012).
34. M. Liu, Z.-R. Cai, S. Hu, A.-P. Luo, C.-J. Zhao, H. Zhang, W.-C. Xu, and Z.-C. Luo, "Dissipative rogue waves induced by long-range chaotic multi-pulse interactions in a fiber laser with a topological insulator-deposited microfiber photonic device," Opt. Lett. **40**, 4767–4770 (2015).
35. Z. Cai, M. Liu, S. Hu, J. Yao, A. Luo, Z. Luo, and W. Xu, "Graphene-decorated microfiber photonic device for generation of rogue waves in a fiber laser," IEEE J. Sel. Top. Quantum Electron. **23**, 20–25 (2017).
36. Z.-C. Luo, M. Liu, A.-P. Luo, and W.-C. Xu, "Two-dimensional materials-decorated microfiber devices for pulse generation and shaping in fiber lasers," Chin. Phys. B **27**, 094215 (2018).
37. B. Zhang, G. Sun, S. Ding, H. Asakura, J. Zhang, P. Sautet, and N. Yan, "Atomically dispersed Pt_1–polyoxometalate catalysts: how does metal-support interaction affect stability and hydrogenation activity?" J. Am. Chem. Soc. **141**, 8185–8197 (2019).
38. X. Chen, B. Zhang, Y. Wang, and N. Yan, "Valorization of renewable carbon resources for chemicals," CHIMIA Int. J. Chem. **69**, 120–124 (2015).
39. X. Ren, Z. Li, Z. Huang, D. Sang, H. Qiao, X. Qi, J. Li, J. Zhong, and H. Zhang, "Environmentally robust black phosphorus nanosheets in solution: application for self-powered photodetector," Adv. Funct. Mater. **27**, 1606834 (2017).
40. B. Zhang, H. Asakura, J. Zhang, J. Zhang, S. De, and N. Yan, "Stabilizing a platinum1 single-atom catalyst on supported phosphomolybdic acid without compromising hydrogenation activity," Angew. Chem. Int. Ed. **55**, 8319–8323 (2016).
41. M. Pawar, S. Kadam, and D. J. Late, "High-performance sensing behavior using electronic ink of 2D $SnSe_2$ nanosheets," ChemistrySelect **2**, 4068–4075 (2017).
42. T. Pei, L. Bao, G. Wang, R. Ma, H. Yang, J. Li, C. Gu, S. Pantelides, S. Du, and H.-J. Gao, "Few-layer $SnSe_2$ transistors with high on/off ratios," Appl. Phys. Lett. **108**, 053506 (2016).
43. H. Zhang, D. Y. Tang, L. M. Zhao, and N. Xiang, "Coherent energy exchange between components of a vector soliton in fiber lasers," Opt. Express **16**, 12618–12623 (2008).
44. M. Jung, J. Lee, J. Park, J. Koo, Y. M. Jhon, and J. H. Lee, "Mode-locked, 1.94-μm, all-fiberized laser using WS_2-based evanescent field interaction," Opt. Express **23**, 19996–20006 (2015).
45. Y. Zhou, Z. Zhang, W. Jiang, P. Gao, X. Zhang, W. Zhang, Y. Zhang, A. Qyyum, X. Li, M. Liao, and W. Gao, "A passively mode-locked thulium-doped fiber laser based on a D-shaped fiber deposited with PbS nanoparticles," J. Mater. Chem. C **7**, 11215–11219 (2019).
46. T. Wang, W. Ma, Q. Jia, Q. Su, P. Liu, and P. Zhang, "Passively mode-locked fiber lasers based on nonlinearity at 2-μm band," IEEE J. Sel. Top. Quantum Electron. **24**, 1102011 (2018).
47. Z. Wang, H. Li, M. Luo, T. Chen, X. Xia, H. Chen, C. Ma, J. Guo, Z. He, Y. Song, J. Liu, X. Jiang, and H. Zhang, "MXene photonic devices for near-infrared to mid-infrared ultrashort pulse generation," ACS Appl. Nano Mater. **3**, 3513–3522 (2020).
48. Q. Wang, T. Chen, B. Zhang, M. Li, Y. Lu, and K. P. Chen, "All-fiber passively mode-locked thulium-doped fiber ring laser using optically deposited graphene saturable absorbers," Appl. Phys. Lett. **102**, 131117 (2013).
49. J. Sotor, G. Sobon, M. Kowalczyk, W. Macherzynski, P. Paletko, and K. M. Abramski, "Ultrafast thulium-doped fiber laser mode locked with black phosphorus," Opt. Lett. **40**, 3885–3888 (2015).
50. K. Yin, B. Zhang, L. Li, T. Jiang, X. Zhou, and J. Hou, "Soliton mode-locked fiber laser based on topological insulator Bi_2Te_3 nanosheets at 2 μm," Photon. Res. **3**, 72–76 (2015).
51. J. Wang, W. Lu, J. Li, H. Chen, Z. Jiang, J. Wang, W. Zhang, M. Zhang, I. L. Li, Z. Xu, W. Liu, and P. Yan, "Ultrafast thulium-doped fiber laser mode locked by monolayer WSe_2," IEEE J. Sel. Top. Quantum Electron. **24**, 1100706 (2018).
52. M. Zhang, J. Li, H. Chen, J. Zhang, J. Yin, T. He, J. Wang, M. Zhang, B. Zhang, J. Yuan, P. Yan, and S. Ruan, "Group IIIA/IVA monochalcogenides nanosheets for ultrafast photonics," APL Photon. **4**, 090801 (2019).
53. J. Guo, Z. Wang, R. Shi, Y. Zhang, Z. He, L. Gao, R. Wang, Y. Shu, C. Ma, Y. Ge, Y. Song, D. Fan, J. Xu, and H. Zhang, "Graphdiyne as a promising mid-infrared nonlinear optical material for ultrafast photonics," Adv. Opt. Mater. **8**, 2000067 (2020).